PCCP

ROYAL SOCIETY OF CHEMISTRY

PAPER

View Article Online
View Journal | View Issue



Cite this: *Phys. Chem. Chem. Phys.*, 2020, **22**, 17385

# Ultrafast dynamics of exciton formation and decay in two-dimensional tungsten disulfide (2D-$WS_2$) monolayers

Zeynep Ezgi Eroglu,[a] Olivia Comegys,[a] Leo S. Quintanar,[a] Nurul Azam,[b] Salah Elafandi,[b] Masoud Mahjouri-Samani[b] and Abdelaziz Boulesbaa *[a]

Excitons in two-dimensional transition metal dichalcogenide monolayers (2D-TMDs) are of essential importance due to their key involvement in 2D-TMD-based applications. For instance, exciton dissociation and exciton radiative recombination are indispensible processes in photovoltaic and light-emitting devices, respectively. These two processes depend drastically on the photogeneration efficiency and lifetime of excitons. Here, we incorporate femtosecond pump–probe spectroscopy to investigate the ultrafast dynamics of exciton formation and decay in a single crystal of monolayer 2D tungsten disulfide ($WS_2$). Investigation of the formation dynamics of the lowest exciton ($X_A$) indicated that the formation time linearly increases from ~150 fs upon resonant excitation, to ~500 fs following excitation that is ~1.1 eV above the band-gap. This dependence is attributed to the time it takes highly excited electrons in the conduction band (CB) to relax to the CB minimum (CBM) and contribute to the formation of $X_A$. This is confirmed by infrared measurements of electron intraband relaxation dynamics. Furthermore, pump–probe experiments suggested that the $X_A$ ground state depletion recovery dynamics depend on the excitation energy as well. The average recovery time increased from ~10 ps in the case of resonant excitation to ~50 ps following excitation well above the band-gap. Having the ability to control whether generating short-lived or long-lived electron–hole pairs in 2D-TMD monolayers opens a new horizon for the application of these materials. For instance, long-lived electron–hole pairs are appropriate for photovoltaic devices, but short-lived excitons are more beneficial for lasers with ultrashort pulses.

Received 15th June 2020,
Accepted 20th July 2020

DOI: 10.1039/d0cp03220d

rsc.li/pccp



## Introduction

An exciton is a hydrogen-like quasiparticle where a negatively charged electron is bound to a positively charged hole.[1] The dissociation and recombination phenomena of excitons are the engine of many applications, such as photovoltaic and light-emitting devices.[2–9] For instance, the electron–hole recombination is at the origin of photoluminescence (PL), and charge transfer upon the separation of excitons is indispensable for the light-to-energy conversion process in solar cells.[10–13] One class of materials where excitons have been the subject of various investigations is two-dimensional transition metal dichalcogenide monolayers (2D-TMDs).[2–5] This is due to the extraordinarily strong Coulomb interaction resulting from the high geometrical confinement and weak dielectric screenings present in 2D-TMDs.[4,14] The main excitons in 2D-TMDs arise from transitions between spin–orbit split (SOS) levels at the conduction band minimum (CBM) and valence band maximum (VBM) at the *K*-point.[15] One of the best ways of characterizing excitons is the measuring of their dynamics, which reveals and identifies the various recombination channels. Several previous studies of exciton dynamics in 2D-TMD monolayers have indicated that the lowest exciton decays through fast and slow channels.[16–19] For instance, temperature and pump-fluence dependent studies of exciton dynamics suggested that thermalization and relaxation take place within the first ~2 ps, whereas defect assisted recombination is a slower decay-channel.[17,18]

In most exciton-based applications of semiconductors, lowest excitons are of great importance. For instance, these excitons are the main source of PL and charge transfer, which are indispensable for photovoltaic and light emitting devices. Understanding the formation mechanisms and decay pathways of these excitons is essential for improving the optical and electronic functionalities of 2D-TMD-based devices. In a recent report by Steinleitner *et al.*, field-resolved optical pump/mid-infrared probe spectroscopy experiments indicated that

[a] *Department of Chemistry & Biochemistry, California State University, Northridge, 18111 Nordhoff Street, Northridge, 91330 CA, USA. E-mail: aboules@csun.edu*
[b] *Department of Electrical and Computer Engineering, Auburn University, Auburn, AL 36849, USA*

identifying the densities of photoexcited unbound electron–hole pairs and excitons suggest that non-resonant excitation of tungsten diselenide ($WSe_2$) monolayers, up to 60% of photo-generated charge carriers form excitons on a sub-picosecond time-scale.[20] In this report we employ femtosecond pump–probe spectroscopy in the visible and infrared (IR) to investigate the formation and decay ultrafast dynamics for the lowest exciton ($X_A$) in a single crystal of 2D tungsten disulfide ($WS_2$) monolayer. An excitation energy-dependent study of the interband transitions suggested that the formation time of the lowest allowed exciton $X_A$ increases linearly from ~150 fs to ~500 fs when the excitation photon-energy increased from ~2.0 eV to ~3.1 eV. The exciton decay time, measured as the depletion recovery average time in pump–probe experiments, is found to increase linearly from ~10 ps to ~ 50 ps when the excitation energy increases from ~2.0 eV to ~ 2.5 eV, but this decay time remains around 50 ps even when the excitation energy increases to ~3.1 eV. Measurements of intraband relaxation dynamics suggested that electrons resulting from resonant excitation relax in the CB about four times faster than those resulting from excitation well above the band-gap. Having the ability to control whether forming bound or unbound electron–hole pairs in 2D-TMD monolayers opens a new horizon for the application of these materials. For instance, long-lived and easily dissociable unbound electron–hole pairs are appropriate for photovoltaic devices, but short-lived excitons are more suitable to platform pulsed ultrafast lasers.

## Materials and methods

### Subject material

Monolayers of $WS_2$ on fused silica substrates are prepared according to the previously reported laser-assisted synthesis technique (LAST).[21] Briefly, stoichiometric powders were placed inside a graphite boat ($1.2 \times 0.7 \times 0.7$ cm$^3$), and irradiated with a continuous-wave $CO_2$ laser with 10.6 μm wavelength to heat the graphite boat and evaporate the powders. The substrate is placed upside down at 6 mm right above the graphite boat to capture the vapor. The graphite boat and the substrate are placed inside a 1 inch furnace tube to maintain the constant growth environment for targeted 2D crystals. Before starting the growth process, the tube furnace was pumped down to a few millitorrs. Subsequently, Argon gas flow used to remove the remaining air residues from the tube. The background pressure adjusted to 150 Torr during the growth process, and the furnace temperature set to 750 °C. After reaching the desired furnace temperature, the graphite boat was irradiated by 35 W laser power for 90 seconds. Then, the laser and tube furnace were turned off simultaneously and let the system cool naturally to room temperature.

## Spectroscopy methods

### Steady state PL spectroscopy and Raman mappings

A customized optical spectroscopy system is used to measure Raman and PL spectra and maps of 2D-$WS_2$ monolayers. A continuous-wave 532 nm laser is used as an excitation source. In addition, a Horiba HR spectrometer with 1200 grooves mm$^{-1}$ grating was used for Raman acquisition, while 300 grooves mm$^{-1}$ grating was used for PL. To collect spectra, a confocal microscope with a 50× objective lens (NA = 0.75) is used. For mapping, a 100× objective lens was used to scan the monolayers sample located on an automated XY stage with 0.5 μm step size.

### Femtosecond pump–probe measurements

A scheme representative of the experimental setup for ultrafast spectroscopy measurements is shown in Fig. 1. It is based on a Titanium:Sapphire femtosecond amplifier (Astrella, Coherent Inc), which provides pulses centered at 800 nm, ~35 femtosecond duration, 6 W average power at a repetition rate of 5 kHz. To probe interband transitions in 2D-$WS_2$ monolayers, a small portion of the amplifier's output is used to generate a spectrally broad (460–920 nm) white light supercontinuum (WL) in a 2 mm thick sapphire window. To avoid optical chirp in the spectrally broad WL, a reflective parabolic mirror is used for collimation, and a reflective filter (transmits 800 nm and reflects other wavelengths) is used for the filtration of the 800 nm fundamental laser. Excitation pump at 3.1 eV (400 nm) is generated in a 0.5 mm thin beta barium borate (BBO) crystal by frequency-doubling a portion of the 800 nm fundamental laser. This frequency doubling is done without focusing and collimating lenses to maintain the pulse ultrashort duration, and the residual 800 nm is rejected through a filter that transmits the 800 nm and reflects the 400 nm. To generate tunable pump pulses with photon-energies below 2.6 eV (>470 nm), a portion of the Astrella's output is used to power one optical parametric amplifier (OPA1) which is a TOPAS Prime by Coherent Inc. To probe the intraband dynamics, infrared (IR) pulses tunable from 1150 nm to 5000 nm generated in a second OPA2 (OPerA Solo, Coherent Inc) are used. The time-delay between the pump and the probe (WL or IR) is controlled by scanning a motorized stage (Newport MIMS600CC). The pump and probe beams are brought collinearly into a home-built inverted-upright hybrid microscope based on an Olympus IX71, using various thin (0.5 mm) dichroic filters (transmit the WL probe and reflect the pump). In the case of the IR probe, a silicon window is used as a dichroic filter. To maintain the sub-45 fs temporal resolution, the beams are focused on the sample down to ~5 μm using a 40× reflective objective microscopes (ROB). After the sample, the transmitted probe is collimated using a 35 mm focal-length calcium fluoride ($CaF_2$) lens. When the probe is in the visible to measure interband dynamics, the collimated WL exiting the microscope is focused onto a 100 μm slit entrance of a spectrograph (Horiba iHR320), which is coupled with a CCD (Newton, Andor) equipped with an electron multiplier (EM). In the case of investigating the intraband dynamics, the collimated IR probe exiting the microscope is sent collinearly, in an IR coated silicon window, with the 800 nm (its bandwidth narrowed to ~1 nm using a filter) onto a customized (by HC Photonics Corp) periodically poling lithium niobate/tantalite chip (NLC) to upconvert it into visible through sum-frequency generation (SFG). After filtering out the IR and the 800 nm beams, the SFG is

 

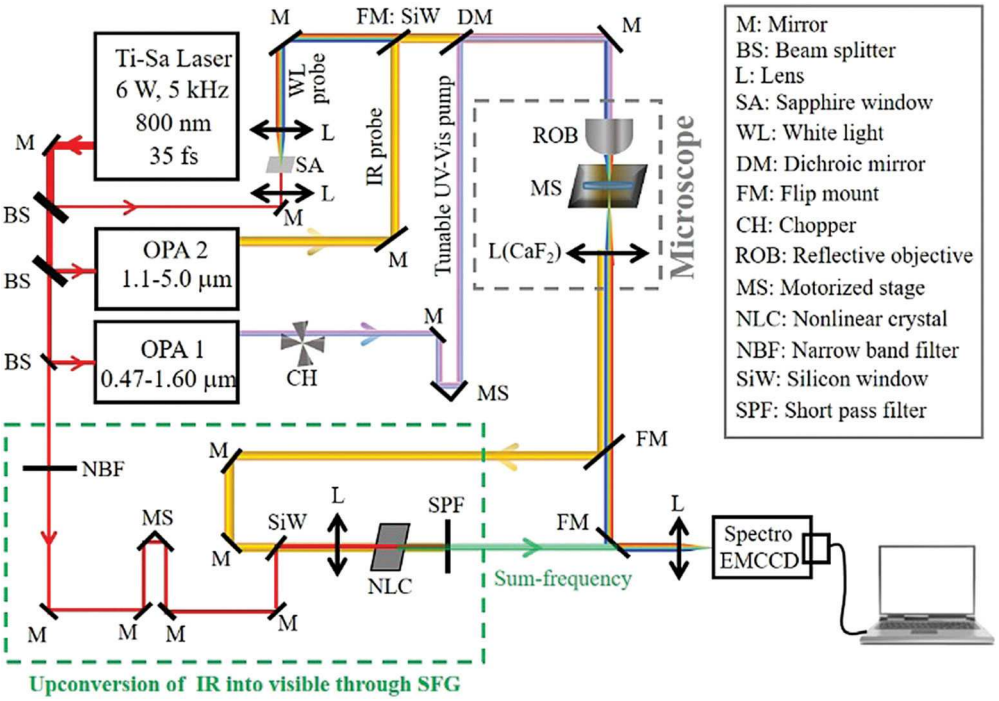


Fig. 1 Scheme representative of the ultrafast spectroscopy/microscopy setup.

focused onto the entrance slit of the spectrograph for detection. To cancel out long-term laser fluctuations, the pump beam passes through an optical chopper set to 100 Hz frequency, and at every time-delay, the absorbance change is calculated between every 50 successive laser shots. In every experiment, four scans over the covered time-delay range are averaged. The instrument response function (IRF) is measured by cross-correlating the pump and probe pulses in a 100 μm thin film of vanadium oxide ($VO_2$) on a sapphire substrate, and suggesting a temporal resolution on the order of ~45 fs for all pump photon-energies used.

In all pump–probe experiments, the pump fluence is kept below ~2 μJ $cm^{-2}$ to avoid photo-damaging the studied 2D-$WS_2$ crystal and many-body interactions.[22,23] However, to generate comparable densities of $X_A$ exciton upon exciting the sample at different photon-energies, the pump fluence is tweaked down using a variable neutral density filter to keep the maximum amplitude of the $X_A$ depletion signal around ~5 mOD for all used excitation photon-energies.

The home-built upright-inverted microscope is equipped with a tungsten halogen light source (HL-2000-LL Ocean Optics) used for measuring the steady-state absorption from the same spot on the monolayer studied in pump–probe experiments.

## Results and discussion

Shown in Fig. 2a is a steady-state absorption spectrum measured from a 2D-$WS_2$ monolayer single crystal. It contains three main peaks assigned to excitonic transitions $X_A$, $X_B$, and $X_C$, superimposed on a "background-like" broad absorption band assigned to the tail of the CB.[24] The two lowest excitons $X_A$ and $X_B$ originate from transitions between the spin–orbit split levels in the VB and CB at the $K$ and $K'$ points of the Brillouin zone.[14,15] The third exciton $X_C$ at higher photon-energies originates from transitions near the $\Lambda$ point in the $k$-space, where the absorbance is amplified due to the nesting effect.[9,25,26] To distinguish the contributions of exciton transitions and the tail of the CB to the measured steady-state absorption, the spectrum is fit to a three-Gaussian function superimposed on a cubic polynomial. The components of the converged fit are shown in Fig. 2b. The values of the fit parameters [center (eV), width (meV), absorbance (OD)] are [2.03, 42.0, 0.030], [2.49, 90.0, 0.014], and [3.04, 120, 0.020] for excitons $X_A$, $X_B$, and $X_C$, respectively.

To confirm that the studied crystals are monolayers, PL and Raman scattering measurements are carried out. Shown in Fig. 3a is a PL map obtained following excitation at 532 nm of an area containing one of the studied crystals on a fused silica substrate. It shows that while there is emission on the crystal, there is no emission outside the 2D-$WS_2$ flake. To gain spectral information, plotted in Fig. 3b is one PL spectrum which consists of a strong peak centered around 630 nm (~1.97 eV), assigned to the direct band-gap emission of the 2D-$WS_2$ monolayer resulting from the radiative recombination of electrons and holes of the lowest exciton $X_A$.[9,27] This monolayer character of the studied crystals is further confirmed by examining the Raman scattering map and spectrum shown in Fig. 3c and d, respectively. The peaks $E^1_{2g}$ and $A_{1g}$ centered at 351 $cm^{-1}$ and 419 $cm^{-1}$ are assigned to in-plane and out-of-plane vibrations, respectively.[28–30]

The strategy of investigating the ultrafast dynamics of the lowest exciton formation, using pump–probe spectroscopy,

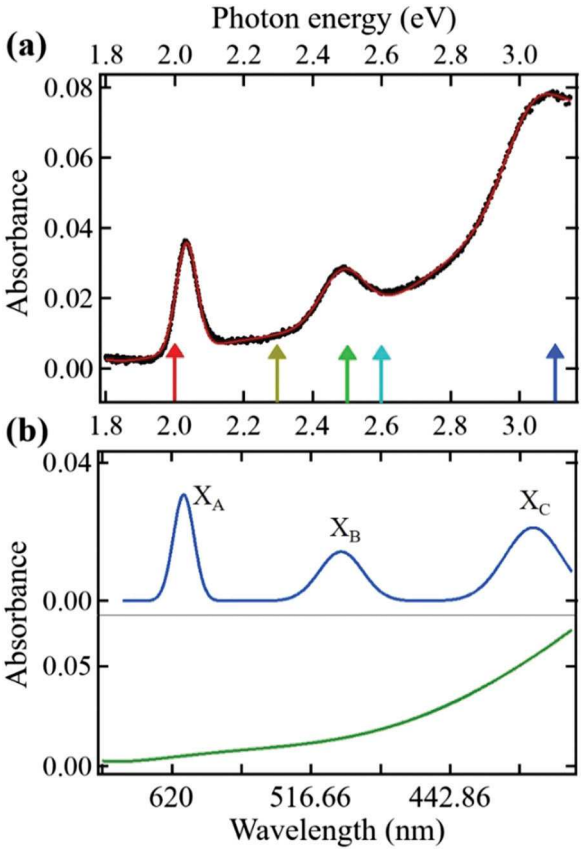


Fig. 2 (a) Steady-state absorption spectrum measured from a 2D-$WS_2$ monolayer single crystal on a fused silica substrate (filled circles). The solid plot is a three-Gaussian superimposed on a cubic polynomial function. The vertical colored arrows indicate the excitation photon-energies used in pump–probe experiments. (b) In the upper panel are the three Gaussian peaks indicating excitons $X_A$, $X_B$, and $X_C$, and in the lower panel is the cubic polynomial components of the fit plotted in (a).

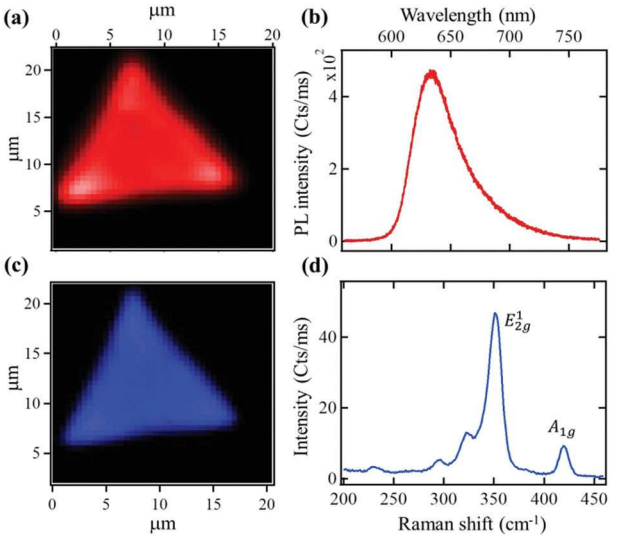


Fig. 3 (a) PL map of the studied 2D-$WS_2$ monolayer crystal measured as the area under the emission spectrum following excitation at 532 nm (2.33 eV). (b) One PL spectrum from (a). (c) Raman intensity map collected from the same 2D-$WS_2$ crystal as in (a) excited at 532 nm, the intensity is the area under the curve over the 325–475 $cm^{-1}$ range. (d) One Raman spectrum from (c) outlining the $E^1_{2g}$ and $A_{1g}$ peaks as indicated.

consists of exciting the 2D-$WS_2$ monolayer resonantly with its lowest exciton $X_A$, and at other photon-energies higher than the band-gap, and in each experiment, we measure the time it takes for the ground-state depletion of the $X_A$ peak ($\sim$2 eV in Fig. 2) to form. We note that unlike in a molecule where the ground state depletion formation is instantaneous and limited by the IRF, in semiconductors there is an extra time corresponding to intraband relaxations of excited electrons in the CB before reaching the level in the CB that is involved in the ground state transition.[15,16,20] In order to obtain an accurate comparison of dynamics when changing the excitation photon-energy, the probe beam is kept on the same spot on the monolayer. The spatial overlap is optimized by tweaking the pump beam direction when the excitation photon-energy is changed. We note that the steady-state absorption spectrum shown in Fig. 2 is measured from the same spot on the monolayer as in the pump–probe measurements.

To demonstrate the general spectral features of transient absorption measurements, we show in Fig. 4a the absorbance changes recorded up to 500 ps following excitation of the 2D-$WS_2$ monolayer crystal at 3.1 eV (400 nm). Transient spectra at 0.5, 2.0, 20, and 100 ps are shown in Fig. 4b. Based on the steady-state absorption spectrum shown in Fig. 2, the negative peaks around 2 eV and 2.4 eV, are assigned to the depletion of excitonic transitions $X_A$ and $X_B$, respectively. The positive broad bands are induced absorptions that can originate from several effects. For instance, they can originate from peak broadening mechanisms,[16] and electrons and excitons excited by the pump pulse may absorb probe photons at different energies to make transitions to higher energy levels in the CB and higher energy excitons.[27]

In order to focus the study on the formation and decay of the $X_A$ ground state depletion, we show in Fig. 5 its dynamics averaged around 2.0 eV ($\sim$620 nm) following excitation at different photon-energies. Although exciton formation and decay are complex processes which cannot be quantified and described explicitly by an exponential function, the net overall exciton population change at different time-delays can be described by a combination of exponential rise and decay components. To account for the temporal widths of the pump and probe pulses, we fit the dynamics shown in Fig. 5 by convoluting a multi-exponential function (one rise and three decay components) with a 45 fs Gaussian IRF, and the returned parameters are listed in Table 1. To focus on the signal formation time, shown in Fig. 5a are the dynamics at early time-delays. Although the signal amplitudes are normalized to the same value because we are interested in comparing the dynamics, the real magnitudes of the $X_A$ depletion signals are kept around 5 mOD by tweaking the pump power down using a variable neutral density filter when switching the excitation energy. Because the number of experimental data points is limited to 20 fs steps around these time-delays, we considered the fit plots (solid lines in Fig. 5a), and in each excitation energy

 

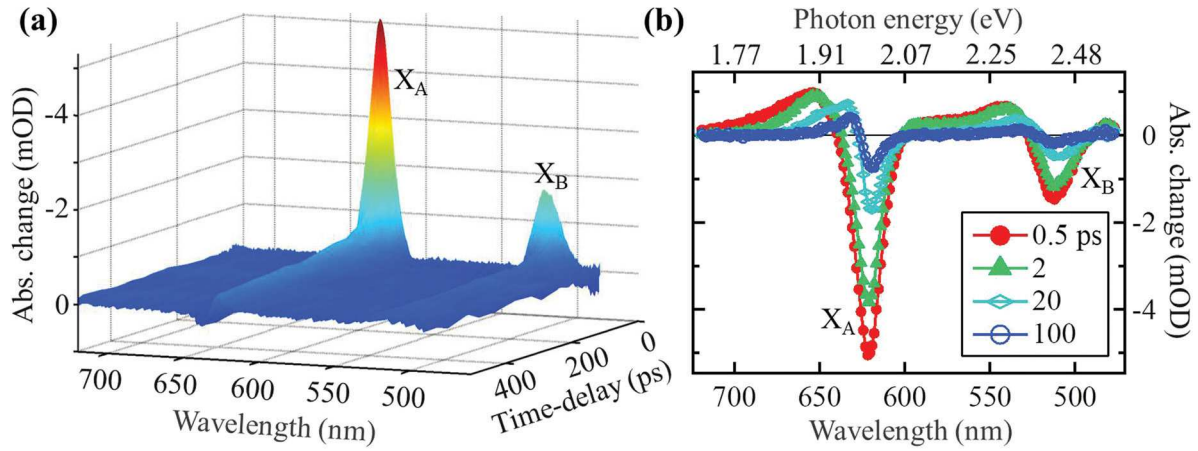


Fig. 4 (a) Transient absorption results following excitation at 3.1 eV (400 nm) of the 2D-$WS_2$ monolayer single crystal on a fused silica substrate. (b) Spectral cuts from (a) at different time-delays as indicated.

case, we calculated the difference between the time-delay at which the depletion signal starts to form (first non-zero amplitude) and that at which the depletion signal reaches its maximum amplitude. These differences are plotted in Fig. 5b. We will call this quantity the exciton formation time (FT). These measurements suggest that the FT depends linearly on the excitation energy. In the case of resonant excitation with respect to the $X_A$ transition, the FT was barely longer than the IRF but, in the case of 3.1 eV excitation, which is ~1.1 eV higher than the band-gap, the FT was about 500 fs. The extra time in the case of exciting the monolayer well above its band-gap represents the time it takes excited electrons in the CB to undergo intraband relaxations before reaching the lowest allowed energy level in the CB to form $X_A$ excitons.[15]

In order to examine the $X_A$ decay, we plot in Fig. 5c its depletion recovery dynamics following excitation at different photon-energies. Before presenting the detailed dependence of each decay component on the excitation energy, we show in Fig. 5d the dependence of the amplitude-weighted average time-constants, calculated as $\sum_i A_i t_i$, on the excitation energy, where $A_i$ and $t_i$ are the amplitude and time constant of the exponential component $i$, respectively. The dependence of the individual time constants $t_1$, $t_2$, and $t_3$ on the excitation energy is shown in the inset of Fig. 5d. This average recovery time (RT) increased from ~10 ps in the case of resonant excitation to ~50 ps in cases where the excitation energy is above the $X_B$ exciton (2.5 eV), and it remained around this value even for the case of 3.1 eV excitation energy. A close examination of the fit parameters indicates that the dynamics are dominated by the fast components in the case of resonant excitation but, in the case of excitation above the band-gap, the dynamics are dominated by the slow components. In fact, only about 30% of the excited population decays with time-constants shorter than ~2 ps in all off-resonance excitation cases but, in the case of resonant excitation, up to ~70% of the excited population decays with time constants on the order of or shorter than ~2 ps (first two exponential decay components). With the exception of the resonant excitation case where the time constant of the second decay component is on the order of ~2 ps and the amplitude percentage is about ~30%, in all other excitation energy cases, the second time-constant varies from ~13 to ~40 ps and the amplitude percentages are ~40%. About a quarter of the excited population in all cases of excitation energies decays through the third component with a time-constant increasing from ~37 ps to ~182 ps.

Several previous studies of exciton dynamics in 2D-TMD monolayers have indicated that the lowest exciton $X_A$ decays through fast and slow channels.[16–19] For instance, studies of exciton dynamics dependence on temperature and pump-fluence suggested that thermalization and relaxation take place within the first ~2 ps, whereas defect-assisted recombination is a slower decay-channel.[17,18] Consequently, we assign $t_1$, $t_2$, and $t_3$ to thermalization, relaxation, and defect-assisted recombination, respectively. This suggests that in the case of resonant excitation, the majority of excited population decays *via* thermalization and relaxation, whereas, upon excitation well above the band-gap, the majority of excited population decays through defect-assisted recombination. Because these processes occur simultaneously and competitively, the measured signals are the net overall outcome, and each time constant indicates which process is the dominant factor at any given time-delay.

The previous discussion is supported further by taking into consideration the steady-state absorption spectrum shown in Fig. 2 in interpreting the pump–probe dynamics. In the case of resonant excitation at ~2 eV, almost all the absorbed photons are consumed through the excitonic transition to directly form $X_A$ excitons, which recombine faster.[20,24] However, in the case of excitations at higher energies, notably beyond ~2.5 eV, an important portion of absorbed photons is consumed for the formation of higher energy excitons (*e.g.* $X_B$ and $X_C$) and unbound electron–hole pairs, which are more vulnerable than bound excitons to trapping at defect sites located below, near and above the band-gap. Because the number of generated unbound electron–hole pairs in the case of excitations well above the band-gap is greater than that in the case of resonant

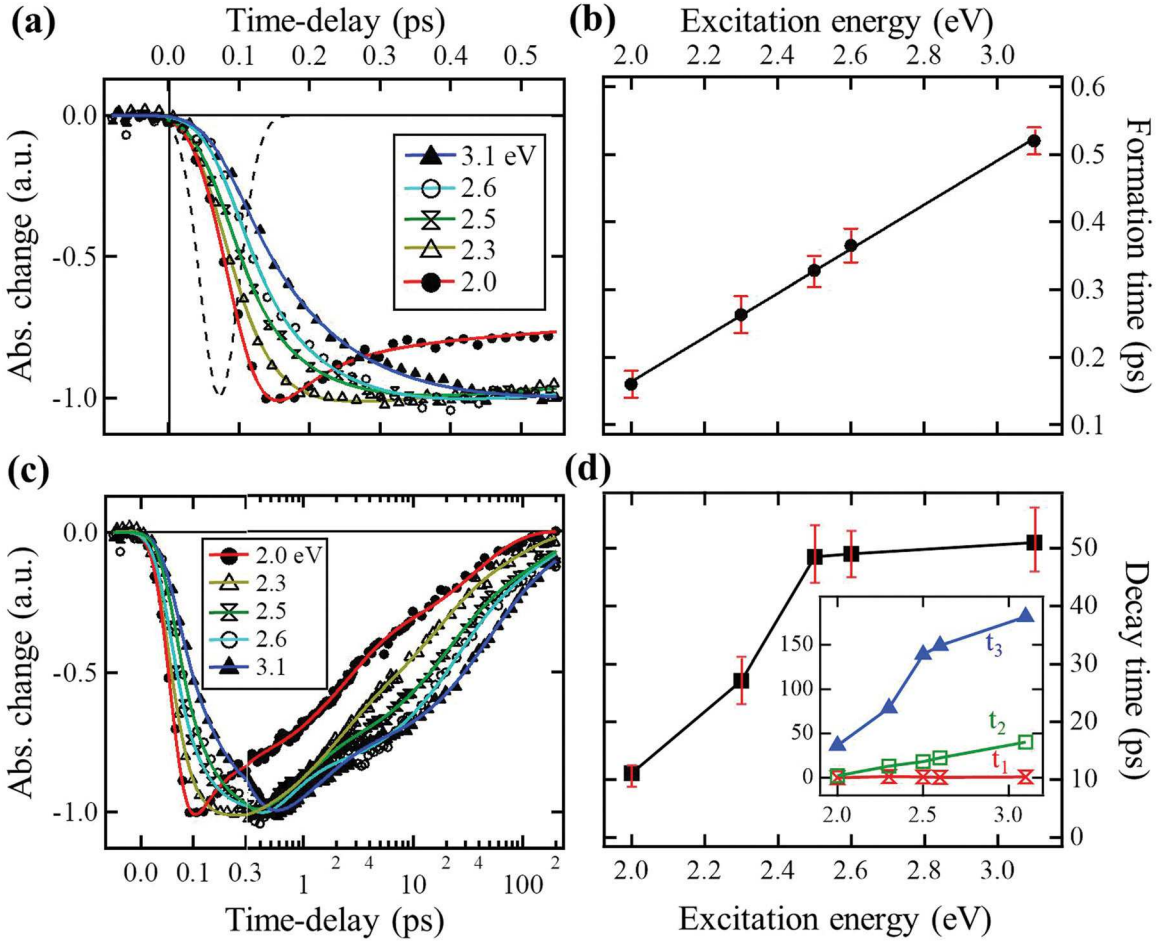


Fig. 5 (a) Early time-delay dynamics of exciton $X_A$ depletion signal recorded at 620 nm following excitation at different photon energies of a 2D-$WS_2$ monolayer single crystal on a fused silica substrate (symbols). The signals are normalized to the same maximum amplitude. Solid lines are fits to a multiexponential decay function convoluted with the instrument response function (dashed line), which is measured from 100 μm thin film of $VO_2$ on a sapphire substrate. (b) The dependence of the $X_A$ depletion formation time on the excitation energy (circles), the solid line is a guide for the eye. Error bars are standard deviations of three different experiments. The values are extracted as the difference between the time-delays when the depletion signals start and when they reach their maxima. (c) Dynamics of $X_A$ depletion recovery signals following excitation at different photon energies as indicated (symbols). Solid plots are fits, and the time-delay axis is shown in a linear scale up to 0.3 ps, and logarithmic scale thereafter. (d) The dependence of $X_A$ depletion average recovery time on the excitation energy (squares), solid lines are guides for the eye. Error bars are standard deviations of three different experiments. The inset shows the dependence of the three time constants on the excitation energy.

Table 1 List of the fit parameters of the $X_A$ exciton depletion recovery dynamics upon excitation at different photon-energies. $A_i$ and $t_i$ are the amplitudes and time constants of the exponential component $i$, respectively. FT is the depletion formation time, and RT is the amplitude weighted average depletion recovery time calculated as $\sum_i A_i t_i$

| Excitation | 2.0 eV | 2.3 eV | 2.5 eV | 2.6 eV | 3.1 eV |
|---|---|---|---|---|---|
| FT (ps) | **0.15** | **0.25** | **0.31** | **0.36** | **0.51** |
| $A_1$ (%) | 40 | 34 | 29.1 | 30.8 | 33.9 |
| $t_1$ (ps) | 0.07 | 1.53 | 0.82 | 0.48 | 1.2 |
| $A_2$ (%) | 32 | 40 | 43.7 | 44.4 | 48.6 |
| $t_2$ (ps) | 2.2 | 13.3 | 18.4 | 22.7 | 40.6 |
| $A_3$ (%) | 28 | 26 | 27.2 | 24.8 | 27.3 |
| $t_3$ (ps) | 36.7 | 79 | 139.1 | 149.4 | 181.8 |
| RT (ps) | **11.1** | **26.2** | **50.7** | **47.3** | **46.1** |

excitation, the tapping sites saturate easier, and consequently, the defect-assisted recombination time, $t_3$, increases with increasing excitation energy as shown in the inset of Fig. 5d.

Furthermore, despite that lattice effects are minimum in 2D-TMDs, these excited charge carriers may transfer energy to phonons during the intraband relaxations, and it is known that this process happens at a longer time-scale.[31]

Experiments to measure the intraband dynamics are conducted using two excitation energies as shown in Fig. 6. The monolayer is excited with ~2.0 eV and ~2.6 eV photon-energies, which are in resonance with and well-above the $X_A$ excitonic transition, respectively. We note that in this experiment it is not convenient to excited at 3.1 eV (400 nm) because the silicon window acting as a dichroic filter absorbs the pump. In both experiments, the intraband relaxation dynamics are probed around 0.66 eV (1880 nm). We note that these IR signals are induced absorptions that originate upon absorption of the IR probe by excited electrons in the CB to make transitions to higher energy levels. For instance, based on the steady-state absorption spectrum shown in Fig. 2, the energy difference

 

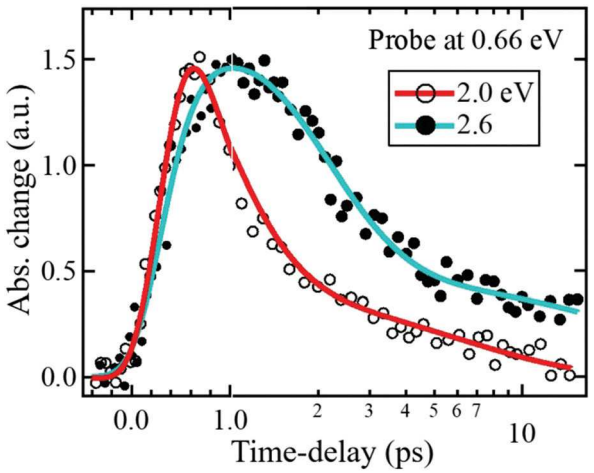


Fig. 6 Intraband dynamics measured around 0.66 eV (~1880 nm) following excitation at two different photon-energies as indicated (symbols). Solid lines are fits to a bi-exponential decay function convoluted with a Gaussian instrument response function. Signals are normalized to the same amplitudes for easier comparison of dynamics. The time-delay axis is shown on a linear scale up to 1 ps, and a logarithmic scale thereafter.

between $X_A$ and $X_C$ is more than 1 eV, consequently, probing intraband transitions at 0.66 eV is possible.

The intraband relaxation dynamics are fit with a bi-exponential decay function, and the returned parameters are listed in Table 2. Although both amplitude-weighted average decay time constants are on the ps time-scale, which is consistent with previous reports,[24] in the case of resonant excitation, the intraband relaxations are about four times faster than in the case where the excitation is well above the band-gap.

In both cases of excitation energy, almost 90% of excited electrons in the CB decay with a time constant on the sub or ~1 ps time-scale, which indicates that this component, $t_1$, likely represents the intraband relaxation of excited electrons in the CB. The remaining small portion of the excited population in the case of excitation well above the band-gap decays with a time constant that is four times longer than that in the case of resonant excitation. Because in both cases of excitation energy the value of $t_2$ is much longer than the time it takes excited electrons to reach the CBM to form the $X_A$ exciton, one may assume that $t_2$ is related to defect-assisted recombination. According to the steady state-absorption spectrum shown in Fig. 2, excitation-photons at 2.6 eV are mostly absorbed by the tail of the CB, leading to the generation of unbound electron–hole pairs,[24,32,33] which are more susceptible to traps, it is likely that $t_2$ represents the recombination of trapped electrons at defect sites located above the CBM with holes in the VB. We note that this recombination is different from the recombination of $X_A$, because in this case the electrons recombine from a trapping site without reaching the CBM.

Table 2 List of the fit parameters of intraband dynamics. $A_i$ and $t_i$ are the amplitudes and time constants of the exponential component $i$, respectively. The decay time (DT) is the amplitude weighted average decay time calculated as $\sum_i A_i t_i$

| | 2.6 eV pump | 2.0 eV pump |
|---|---|---|
| $A_1$ (%) | 88 | 87 |
| $t_1$ (ps) | 1.08 | 0.46 |
| $A_2$ (%) | 12 | 13 |
| $t_2$ (ps) | 30.67 | 5.91 |
| DT (ps) | **4.63** | **1.16** |

Although the dependence of intraband dynamics on the excitation energy is qualitatively similar to that of interband dynamics, quantitatively the time constants are different. This is due to the fact that in the case of interband dynamics, the observed signals (at 2 eV) describe the recombination between electrons and holes located at the CBM and VBM, respectively, which happens after the intraband relaxation whereas, in the case of intraband dynamics, the observed signals describe the presence (relaxations) of excited electrons in the CB.

## Conclusions

In summary, we investigated the ultrafast dynamics of exciton formation and decay in a single crystal of 2D-$WS_2$ monolayers. We incorporated visible pump/visible probe and visible pump/IR probe femtosecond spectroscopies to study interband and intraband transitions, respectively. These investigations indicated that the formation time of the lowest exciton $X_A$ increases linearly from ~150 fs to ~500 fs when the excitation energy increases from 2.0 eV to 3.1 eV, which suggests that this time corresponds to the time it takes excited electrons in the CB to relax to the lowest allowed energy level in the CB to form $X_A$ excitons. These results are confirmed by measurements of intraband relaxation dynamics, which suggest that electrons resulting from resonant excitation relax in the CB about four times faster than those resulting from excitation well above the band-gap.

Investigating the recovery dynamics of the $X_A$ ground-state depletion indicated that the average recovery-time increases linearly from ~10 ps to ~50 ps when the excitation energy increases from 2.0 eV (in resonance with exciton $X_A$) to ~2.5 eV (in resonance with exciton $X_B$), but this average time remains around 50 ps even when the excitation energy increases to ~3.1 eV. This dependence on the excitation energy is explained by the fact that in resonant excitation, most absorbed pump photons are consumed in a direct generation of $X_A$ excitons, which recombine faster, whereas in the case of exciting the monolayer with photon-energies well above its band-gap, an important portion of absorbed pump photons leads to the generation of unbound electron–hole pairs, which decay slower. Furthermore, these electron–hole pairs are more susceptible to defects, which slow down their recombination. Gaining the ability to control whether generating short-lived or long-lived electron–hole pairs in 2D-TMD monolayers opens a new horizon for the application of 2D-TMD materials. For instance, long-lived electron–hole pairs are appropriate for photovoltaic devices, but short-lived excitons are more beneficial for pulsed ultrafast lasers.

## Conflicts of interest

There are no conflicts to declare.

## Acknowledgements

The authors acknowledge support from the National Science Foundation under grant DMR-1828019.

## References

1 R. J. Elliott, Intensity of Optical Absorption by Excitons, *Phys. Rev.*, 1957, **108**, 1384.
2 T. Zhu, J. M. Snaider, L. Yuan and L. Huang, Ultrafast Dynamic Microscopy of Carrier and Exciton Transport, *Annu. Rev. Phys. Chem.*, 2019, **70**, 219–244.
3 B. Kaviraj and D. Sahoo, Physics of excitons and their transport in two dimensional transition metal dichalcogenide semiconductors, *RSC Adv.*, 2019, **9**, 25439–25461.
4 T. Mueller and E. Malic, Exciton physics and device application of two-dimensional transition metal dichalcogenide semiconductors, *npj 2D Mater. Appl.*, 2018, **2**, 29.
5 M. Bernardi, C. Ataca, M. Palummo and J. C. Grossman, Optical and Electronic Properties of Two-Dimensional Layered Materials, *Nanophotonics*, 2016, **5**, 111–125.
6 M. Bernardi, M. Maurizia Palummo and J. C. Grossman, Extraordinary Sunlight Absorption and One Nanometer Thick Photovoltaics Using Two-Dimensional Monolayer Materials, *Nano Lett.*, 2013, **13**, 3664–3670.
7 M. L. Tsai, S. H. Su, J. K. Chang, D. S. Tsai, C. H. Chen, C. I. Wu, L. J. Li, L. J. Chen and J. H. He, Monolayer $MoS_2$ Heterojunction Solar Cells, *ACS Nano*, 2014, **8**, 8317–8322.
8 L. Y. Gan, Q. Zhang, Y. Cheng and U. Schwingenschlögl, Photovoltaic Heterojunctions of Fullerenes with $MoS_2$ and $WS_2$ Monolayers, *J. Phys. Chem. Lett.*, 2014, **5**, 1445–1449.
9 A. Boulesbaa, K. Wang, M. Mahjouri-Samani, M. Tian, A. A. Puretzky, I. Ivanov, C. M. Rouleau, K. Xiao, B. G. Sumpter and D. B. Geohegan, Ultrafast Charge Transfer and Hybrid Exciton Formation in 2D/0D Heterostructures, *J. Am. Chem. Soc.*, 2016, **138**(44), 14713–14719.
10 B. O'Regan and M. Grätzel, A low-cost, high-efficiency solar cell based on dye-sensitized colloidal $TiO_2$ films, *Nature*, 1991, **353**, 737–740.
11 A. Hagfeldt, G. Boschloo, L. Sun, L. Kloo and H. Pettersson, Dye-Sensitized Solar Cells, *Chem. Rev.*, 2010, **110**, 6595–6663.
12 A. Miyata, A. Mitioglu, P. Plochocka, O. Portuga, J. Tse-Wei Wang, S. D. Stranks, H. J. Snaith and R. J. Nicholas, Direct measurement of the exciton binding energy and effective masses for charge carriers in organic–inorganic tri-halide perovskites, *Nat. Phys.*, 2015, **11**, 582–588.
13 A. Boulesbaa, V. E. Babicheva, K. Wang, I. I. Kravchenko, M.-W. Lin, M. Mahjouri-Samani, C. B. Jacobs, A. A. Puretzky, K. Xiao and I. Ivanov, *et al.*, Ultrafast Dynamics of Metal Plasmons Induced by 2D Semiconductor Excitons in Hybrid Nanostructure Arrays, *ACS Photonics*, 2016, **12**(3), 2389–2395.
14 A. Chernikov, T. C. Berkelbach, H. M. Hill, A. Rigosi, Y. Li, O. Burak Aslan, D. R. Reichman, M. S. Hybertsen and T. F. Heinz, Exciton Binding Energy and Nonhydrogenic Rydberg Series in Monolayer $WS_2$, *Phys. Rev. Lett.*, 2014, **113**, 076802.
15 A. Boulesbaa, B. Huang, K. Wang, M.-W. Lin, M. Mahjouri-Samani, C. Rouleau, K. Xiao, M. Yoon, B. Sumpter and A. Puretzky, *et al.*, Observation of two distinct negative trions in tungsten disulfide monolayers, *Phys. Rev. B: Condens. Matter Mater. Phys.*, 2015, **92**, 115443.
16 H. Shi, R. Yan, S. Bertolazzi, J. Brivio, B. Gao, A. Kis, D. Jena, H. G. Xing and L. Huang, Exciton Dynamics in Suspended Monolayer and Few-Layer $MoS_2$ 2D Crystals, *ACS Nano*, 2013, **7**(2), 1072–1080.
17 H. Wang, C. Zhang and F. Rana, Ultrafast Dynamics of Defect-Assisted Electron–Hole Recombination in Monolayer $MoS_2$, *Nano Lett.*, 2015, **15**, 339–345.
18 G. Moody, J. Schaibley and X. Xu, Exciton dynamics in monolayer transition metal dichalcogenides, *J. Opt. Soc. Am. B*, 2016, **33**, C39–C49.
19 Q. Cui, F. Ceballos, N. Kumar and H. Zhao, Transient Absorption Microscopy of Monolayer and Bulk $WSe_2$, *ACS Nano*, 2014, **8**, 2970–2976.
20 P. Steinleitner, P. Merkl, P. Nagler, J. Mornhinweg, C. Schüller, T. Korn, A. Chernikov and R. Huber, Direct Observation of Ultrafast Exciton Formation in a Monolayer of $WSe_2$, *Nano Lett.*, 2017, **17**(3), 1455–1460.
21 N. Azam, Z. Ahmadi, B. Yakupoglu, S. Elafandi, M. K. Tian, A. Boulesbaa and M. Mahjouri-Samani, Accelerated synthesis of atomically-thin 2D quantum materials by a novel laser-assisted synthesis technique, *2D Mater.*, 2019, **7**, 015014.
22 S. Zhang, N. Dong, N. McEvoy, M. O'Brien, S. Winters, N. C. Berner, C. Yim, Y. Li, X. Zhang and Z. Chen, *et al.*, Direct Observation of Degenerate Two-Photon Absorption and Its Saturation in $WS_2$ and $MoS_2$ Monolayer and Few-Layer Films, *ACS Nano*, 2015, **9**(7), 7142–7150.
23 G. Aivazian, H. Yu, S. Wu, J. Yan, D. G. Mandrus, D. Cobden, W. Yao and X. Xu, Many-body effects in nonlinear optical responses of 2D layered semiconductors, *2D Mater.*, 2017, **4**(2), 025024.
24 H. Chen, X. Wen, J. Zhang, T. Wu, Y. Gong, X. Zhang, J. Yuan, C. Yi, J. Lou and P. M. Ajayan, *et al.*, Ultrafast formation of interlayer hot excitons in atomically thin $MoS_2/WS_2$ heterostructures, *Nat. Commun.*, 2016, **7**, 12512.
25 D. Y. Qiu, F. H. da Jornada and S. G. Louie, Optical spectrum of $MoS_2$: many-body effects and diversity of exciton states, *Phys. Rev. Lett.*, 2013, **111**(21), 216805.
26 D. Kozawa, R. Kumar, A. Carvalho, K. Kumar Amara, W. Zhao, S. Wang, M. Toh, R. M. Ribeiro, A. H. Castro Neto and M. Kazunari, *et al.*, Photocarrier relaxation pathway in two-dimensional semiconducting transition metal dichalcogenides, *Nat. Commun.*, 2014, **5**, 4543.
27 J. Bauer, L. S. Quintanar, K. Wang, A. A. Puretzky, K. Xiao, D. B. Geohegan and A. Boulesbaa, Ultrafast Exciton Dissociation at the 2D-$WS_2$ Monolayer/Perovskite Interface, *J. Phys. Chem. C*, 2018, **122**, 28910–28917.
28 W. Zhao, Z. Ghorannevis, K. Kumar Amara, J. R. Pang, M. Toh, X. Zhang, C. Kloc, P. H. Tane and G. Eda, Lattice dynamics in mono- and few-layer sheets of $WS_2$ and $WSe_2$, *Nanoscale*, 2013, **5**, 9677–9683.
29 M. O'Brien, N. McEvoy, D. Hanlon, T. Hallam, J. N. Coleman and G. S. Duesberg, Mapping of Low-Frequency Raman

 

Modes in CVD-Grown Transition Metal Dichalcogenides: Layer Number, Stacking Orientation and Resonant Effects, *Sci. Rep.*, 2016, **6**, 119476.

30 S. Tongay, W. Fan, J. Kang, J. Park, U. Koldemir, J. Suh, D. S. Narang, K. Liu, J. Ji and J. Li, *et al.*, Tuning Interlayer Coupling in Large-Area Heterostructures with CVD Grown $MoS_2$ and $WS_2$ Monolayers, *Nano Lett.*, 2014, **14**, 3185–3190.

31 C. Ruppert, A. Chernikov, H. M. Hill, A. F. Rigosi and T. F. Heinz, The Role of Electronic and Phononic Excitation in the Optical Response of Monolayer $WS_2$ after Ultrafast Excitation, *Nano Lett.*, 2017, **17**, 644–651.

32 A. F. Rigosi, H. M. Hill, Y. Li, A. Chernikov and T. F. Heinz, interlayer interactions in transition metal dichalcogenide heterostructures by optical spectroscopy: $MoS_2/WS_2$ and $MoSe_2/WSe_2$, *Nano Lett.*, 2015, **15**(8), 5033–5038.

33 Z. G. Yu, S. Krishnamurthy and S. Guha, Photoexcited-carrier-induced refractive index change in small bandgap semiconductors, *J. Opt. Soc. Am. B*, 2006, **23**, 2356–2360.